Geologie en Mijnbouw **77:** 161–176, 1999.

Deformation measurements using SAR interferometry: potential and limitations

Roland Klees[1] & Didier Massonnet[2]
[1]*Delft Institute for Earth Oriented Space Research, Faculty of Civil Engineering & Geoscience, Delft University of Technology, Thijsseweg 11, 2629 JA Delft, the Netherlands;* [2]*Centre National d'Etudes Spatiales, DGAT/SH/QTIS, 18 Avenue E. Belin, 31407 Toulouse CEDEX 4, France*

Received 15 April 1997; accepted in revised form 17 December 1998

Key words: anthropogenic processes, crustal dynamics, earthquake research, glacier and icesheet monitoring, volcano monitoring

Abstract

Most applications of Synthetic Aperture Radar (SAR) make only use of the amplitude information in just one image. Interferometric SAR (InSAR) makes use mainly of the phase measurements in two or more SAR images of the same scene, acquired at two different moments and/or at two slightly different locations. By interference of the two images, very small slant-range changes of the same surface can be inferred. These slant-range changes can be related to topography and/or surface deformations. InSAR thus has the potential of mapping centimeter-scale ground displacements over a region many tens of kilometers in size at a resolution of a few meters making it one of the most promising space-geodetic techniques for monitoring Earth's surface deformations. The goal of this paper is to discuss some of the potential new applications of InSAR for the monitoring of deformations, and to show its major limitations. Some potential new applications of InSAR related to surface-change detection including earthquake and crustal studies, the monitoring of volcanoes and anthropogenic effects, and the monitoring of glaciers and ice sheets are presented. The discussion on the limitations of InSAR for surface-change detection focuses on atmospheric perturbations and the problem of temporal decorrelation.

Introduction

About 40 years ago it was observed that a side-looking imaging radar operating on wavelengths in the order of centimeters can be used to map the Earth's surface with a resolution of some meters without requiring huge antennas. Already NASA's Seasat-A, launched in 1978, and, since 1991, ESA's ERS-1, showed a wide variety of applications of this technique, which is called Synthetic Aperture Radar (SAR). Examples are the study of geological structures and the classification of rock types, the study of ocean waves and currents, and of the characteristics of ice, the detection of ship wakes, and the mapping of land use. The use of SAR as an interferometer, the so-called SAR interferometry (InSAR), is rather new due to the stringent requirements to the stability of the satellite orbit. InSAR offers the possibility to map the Earth's land and ice topography and to measure small displacements over large temporal and spatial scales with subcentimeter accuracy, independently of the Sun's illumination and the cloud coverage. These properties make InSAR a unique technique which combines the high accuracy of classical geodetic techniques such as GPS and leveling with the imaging property of classical remote sensing techniques. Recent examples have demonstrated that InSAR can be applied to study a variety of deformation processes, e.g. land subsidence due to mining activities and due to the withdrawal of water, gas and oil, the co-seismic and post-seismic displacement field related to earthquakes, the deflation and inflation of volcanoes, the dynamics of glaciers and ice sheets, tectonic processes, orogenesis and erosion, and coastal-zone changes.

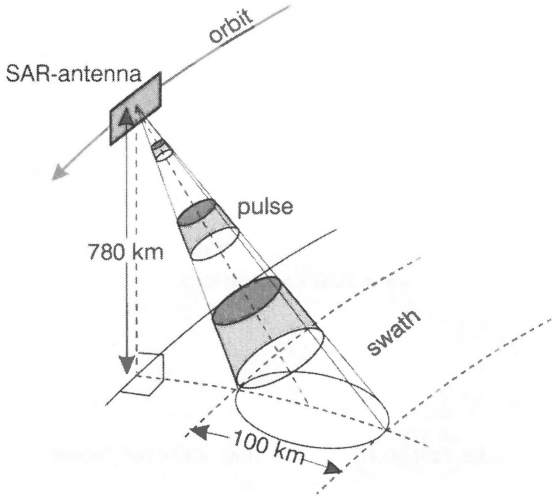

Figure 1. Geometry of an imaging radar. Explanation in text 'Basic principles'. (For full colour reproduction of this figure, see Appendix at the end of this issue.)

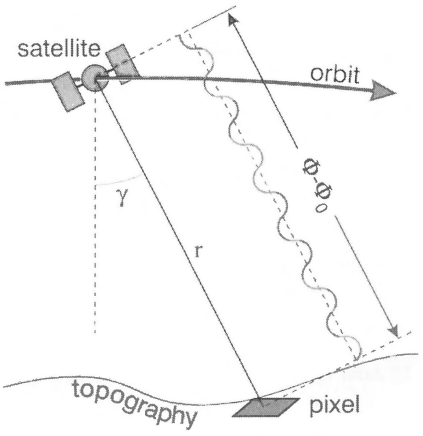

Figure 2. Slant range – phase relation. (For full colour reproduction of this figure, see Appendix at the end of this issue.)

The goal of this paper is to discuss some of the potential new applications of InSAR for the monitoring of deformations, and to show its major limitations. First, a brief review will be given of the basic principles of InSAR as far as needed to understand the applications and the limitations. Some potential new applications of InSAR related to surface-change detection is subsequently presented as to be applicable to earthquake and crustal studies, the monitoring of volcanoes and anthropogenic effects, and the monitoring of glaciers and ice sheets. The limitations of InSAR for surface-change detection with main focus on atmospheric perturbations and the problem of temporal decorrelation are presented thereafter.

The interferometric processing of SAR signals allows not only to infer surface changes from the radar images. InSAR can also be used to derive high-resolution digital elevation maps. Other potential new applications are e.g. the study of the electrical properties of the Earth's surface, including water content, land classification, and the mapping of flooded areas. These aspects will be out of the scope of this paper.

Basic principles

A SAR is an imaging radar device that images the radar backscatter of the Earth's surface. We may think of an antenna, mounted on a spacecraft, which transmits periodically pulses in a side-looking direction with respect to the spacecraft's direction of travel. A part of the radar pulse energy is backscattered from the surface of the Earth and received a fraction of a second later at the same antenna. The brightness (amplitude), the round-trip time (slant-range), and the phase relative to a stable reference oscillator are measured and recorded to construct the image (Figure 1).

The typical size of the illuminated area is about 100 km^2 for today's spacecraft systems. The nominal resolution in the direction of illumination, the so-called range direction, is about 9 m, and in the direction of the spacecraft's motion, the azimuth direction, it is about 5 m. The resolution on the ground depends on the look angle γ (cf. Figure 2). Assuming $\gamma = 23°$, which corresponds to the mean look angle of ERS-1 and ERS-2, we obtain a resolution cell of about 25×5 m^2. Usual applications of SAR make only use of the amplitude information in just one image. InSAR, however, makes use mainly of the phase measurements in two or more SAR images of the same scene, acquired at two different instants and/or at two slightly different locations. By interference of the two images, we can infer very small slant-range changes in two SAR images of the same surface. These slant-range changes can be related to topography and/or surface deformations. Since SAR is an imaging system, we obtain information for each pixel. One full scene contains roughly 10^8 pixels, meaning that SAR provides an almost continuous picture of the topography and/or the deformation field within the scene.

To get an idea how it works let us first look at the relation between the (total) phase Φ and the dis-

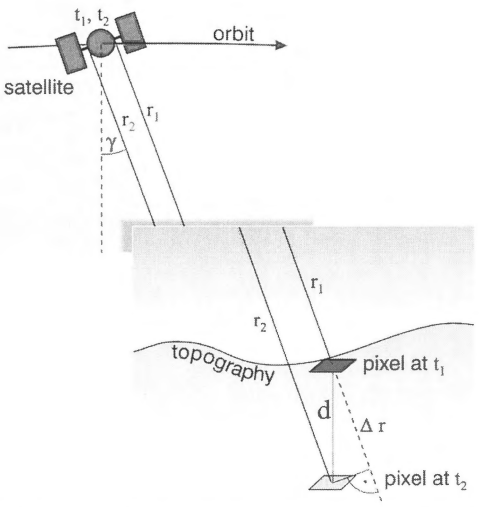

Figure 3. Geometry of InSAR with zero baseline. (For full colour reproduction of this figure, see Appendix at the end of this issue.)

tance between antenna and pixel, the slant-range r. It is given by the simple formula (cf. Figure 2):

$$\Phi = 2\pi \frac{2r}{\lambda} + \Phi_o. \tag{1}$$

That means, the total phase Φ at each point is equal to the sum of a propagation part, proportional to the round-trip distance $2r$, and a scattering part Φ_o due to the interaction of the wave with the ground. The radar wavelength is denoted by λ, which is, e.g. 5.66 cm for the ERS-1 and the ERS-2 SAR. The scattering part Φ_o can never be determined and remains unknown. Therefore, when making use of just one image, the slant-range cannot be inferred from the measured phase due to the unknown phase shift Φ_o. Now, let us assume that two images are taken of the same scene at two distinguished time instants t_1 and t_2 from exactly the same location in space (Figure 3). If the elementary scatterers within each pixel are undisturbed in the time between the two image acquisitions, the scattering part Φ_o does not change. Thus, the phase difference is independent of the scattering mechanism, and becomes a measure of the line-of-sight component Δr of the target displacement vector over the time interval $[t_1, t_2]$:

$$\Delta\Phi = 2\pi \frac{2\Delta r}{\lambda}. \tag{2}$$

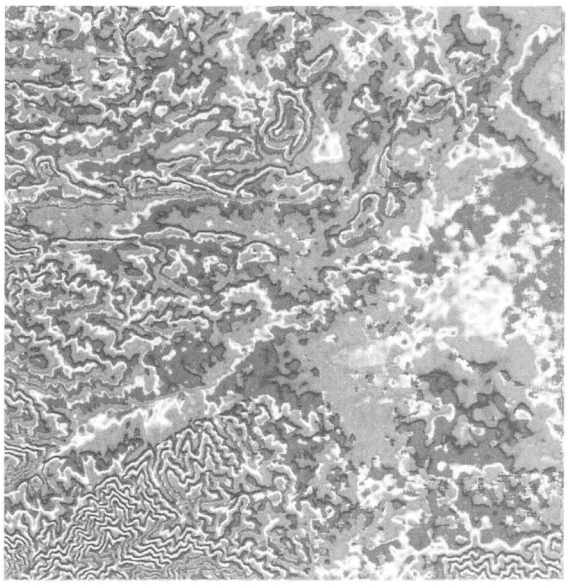

Figure 4. Fractional phase difference image (interferogram) from an area near Perpignan, France. The interferogram is dominated by the topographic fringes from the nearby Pyrenees mountain range. It also contains a contribution from a small earthquake that struck the area in January 1996, and various, small contributions from atmospheric delays. North to the top; scale is 100 m a pixel; area covered is ca. 50 × 50 km. (For full colour reproduction of this figure, see Appendix at the end of this issue.)

So, given the phase difference $\Delta\Phi$, we can, pixel-by-pixel, estimate the component Δr of the displacement in range direction. Since the phase can be measured precisely to a fraction of the radar wavelength, this component can be estimated with a precision of a few millimeters for today's satellite SAR systems.

In fact, the phase difference $\Delta\Phi$ can be measured only modulo 2π, the so-called fractional phase difference $\Delta\Phi_{\text{frac}}$:

$$\Delta\Phi = \Delta\Phi_{\text{frac}} + 2\pi N. \tag{3}$$

The integer number N of complete cycles has to be determined separately to infer the phase difference.

The fractional phase difference image is called interferogram. It shows pixel-by-pixel the fractional phase difference of the complete scene. An example in Figure 4 shows an area roughly 50 km wide and located near the city of Perpignan in southern France. The fractional phase difference is coded on a color wheel. One run through the color wheel corresponds to a complete rotation of 2π or 360° in phase difference. When adding for each pixel the correct multiple of 2π, we obtain the total phase difference for each pixel. In

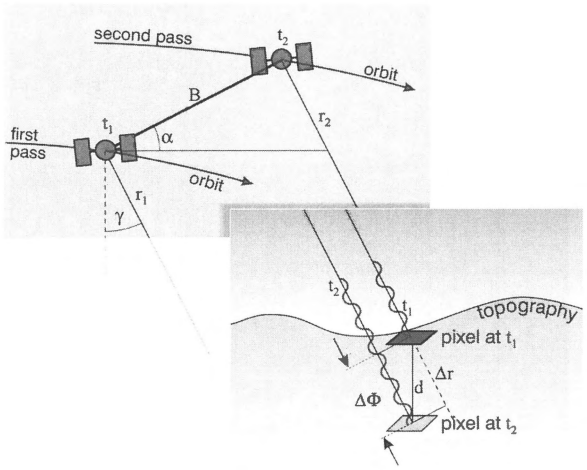

Figure 5. Geometry of InSAR with non-zero baseline. Explanation in text 'Basic principles'. (For full colour reproduction of this figure, see Appendix at the end of this issue.)

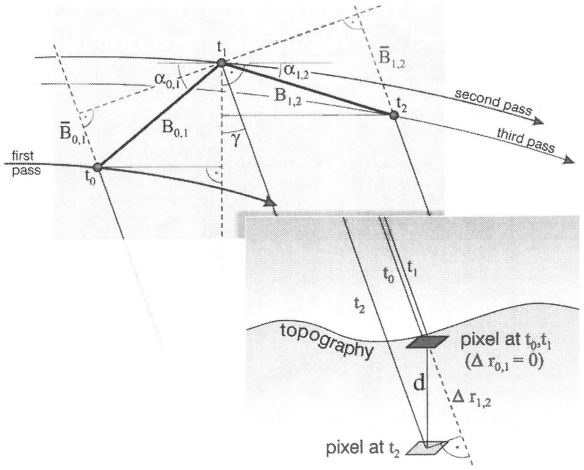

Figure 6. Geometry of differential InSAR. (For full colour reproduction of this figure, see Appendix at the end of this issue.)

reality, however, it is not possible to take the second image at exactly the same location as the first one. That means, the distance between the spacecraft's location at time instants t_1 and t_2, the so-called baseline, is different from zero (Figure 5). Then, the total phase difference $\Delta\Phi$ contains not only the radar line-of-sight component Δr of the displacement vector but also two additional terms that scale with the baseline:

$$\Delta\Phi = \frac{4\pi}{\lambda} \times \left(\Delta r + B \sin(\alpha - \gamma) + B \frac{\cos(\alpha - \gamma)}{R \sin \gamma} h \right). \quad (4)$$

These two terms must be removed to leave the deformation term Δr. The first term is easy to calculate if the baseline and the SAR geometry are known. The second term, however, is due to the topography. To remove it we need additional information, either a high-resolution digital terrain model, i.e. information on h, or a third radar image of the scene. The former is called two-pass InSAR, the latter three-pass or differential InSAR. If a digital elevation model of the terrain is available we can calculate the contribution of the topography to the phase difference $\Delta\Phi$, and the remaining phase difference is only due to the line-of-sight component of the displacement. If a third image of the scene is available, acquired at time say t_0, we can form two image pairs, e.g. a first pair using the images acquired at time t_0 and t_1, and a second pair using the images acquired at time t_1 and t_2. Substitution in Equation (4) and neglecting terms of order $O\left(\frac{h}{R}\right) = O(10^{-3})$ we obtain

$$\Delta r_{1,2} - \Delta r_{0,1} \frac{\bar{B}_{1,2}}{\bar{B}_{0,1}} = \frac{\lambda}{4\pi} \left(\Delta\Phi_{1,2} - \Delta\Phi_{0,1} \frac{\bar{B}_{1,2}}{\bar{B}_{0,1}} \right). \quad (5)$$

$\bar{B}_{0,1}$ and $\bar{B}_{1,2}$ are the components of the baseline parallel to the look direction in the images acquired at t_1 and t_2, respectively (cf. Figure 6). Obviously, the topography term has vanished. When assuming that no surface deformation took place in the time interval $[t_0, t_1]$, $\Delta r_{0,1} = 0$, and Equation (5) provides the deformation $\Delta r_{1,2}$ over the time interval $[t_1, t_2]$:

$$\Delta r_{1,2} \approx \frac{\lambda}{4\pi} \left(\Delta\Phi_{1,2} - \Delta\Phi_{0,1} \frac{\bar{B}_{1,2}}{\bar{B}_{0,1}} \right). \quad (6)$$

Equation (6) is the fundamental equation for detecting and measuring surface-changes with InSAR. Some remarks concerning this equation should be made (cf. Dixon 1995):

1. The phase difference provides only the line-of-sight component of the three-dimensional surface-displacement vector. When using images of both the ascending and descending passes of the satellite, it is possible to extract two components, since, these two interferograms represent views of the same scene taken in two different directions.
2. A phase comparison of the two images cannot be done in all cases but depends on the nature of the

change. For instance, random motions of the scatterers within a pixel introduce noise in the measured phase difference. When the root-mean-square (RMS) motion exceeds the radar wavelength (typically some centimeters), the noise may exceed the signal, meaning that a pixel-by-pixel phase comparison between the two images is not possible. However, if the entire surface within a pixel deforms homogeneously, while the relative motion of the elementary scatterers is small compared to the radar wavelength, the information on the deformation can be extracted from the phase difference.

3. The radar-scattering characteristics within each pixel must not change strongly over the time interval within which the two images have been acquired. Only then, the unknown phase shift Φ_o, which is caused by the interaction of the electromagnetic wave with the ground, is constant over the time interval $[t_1, t_2]$, and drops out when forming the phase difference. When this condition is not met, we term it temporal decorrelation. It constitutes one of the major problems for InSAR. Vegetation, wind effects, soil moisture, snow fall, farming activities etc. preclude or hamper the phase comparison of the two SAR images.
4. As mentioned before, we can measure the total phase difference $\Delta\Phi$ only modulo 2π. Therefore, a proper interpretation of the deformation field requires that for each pixel the fractional phase difference is converted to the total phase difference. The corresponding process is called phase unwrapping. It is comparable to the problem of ambiguity estimation in GPS phase measurements. Phase unwrapping is a rather difficult step that depends e.g. on the imaging geometry, the terrain, and the phase noise level. Note also that if no digital elevation model is available, and two image pairs are used to extract the target displacement, a phase unwrapping of each of the two interferograms is mandatory, unless an appropriate integer combination of the interferograms drastically reduces the topographic contribution.
5. Really large displacements cannot be detected with InSAR. There is a limit with respect to the displacement gradient between adjacent pixels which must be less than half the radar wavelength. This is about 2.8 cm in range for ERS-2.
6. Measuring the surface displacement field to a precision of a fraction of the radar wavelength, i.e. to some millimeter accuracy, requires a relatively accurate a priori estimate of topography in the region. Since the topography may be poorly known, the question arises how sensitive the phase difference $\Delta\Phi$ is to topography. Simple calculations show that the rms phase error that arises from the topographic height error is

$$\sigma_{\Delta\Phi} = \frac{4\pi}{\lambda}\left(\sigma_{\Delta r} + \frac{B\perp}{R \sin\gamma}\sigma_h\right). \qquad (7)$$

$B\perp$ is the baseline component normal to the line-of-sight direction, the so-called effective baseline length. For instance, in case of ERS-2 we obtain (nominal ERS-2 SAR parameters λ = 5.66 cm, R = 850 km, γ = 23°):

$$\sigma_{\Delta\Phi[mm]} \leq 1000\ \sigma_{\Delta r[mm]} + \\ +\ 3.0 \cdot 10^{-6} B\perp_{[m]}\sigma_{h[m]}\ . \qquad (8)$$

For instance, assuming an effective baseline of $B\perp$ = 100 m, a 1-m height error gives a phase difference signature of about 3.8°, equivalent to 0.3 mm line-of-sight displacement, a value well below the expected accuracy of InSAR. Equation (8) also implies that topographic data accurate to about 30 m are required if we want to measure surface-changes at the 1-cm level using image pairs with an effective baseline of $B\perp$ = 100 m. However, the sensitivity of the phase difference with respect to height errors increases proportionally to the effective baseline length, implying that image pairs with short baselines should be chosen to reduce the effect of the unmodeled topography on the deformation. The sensitivity of the phase difference with respect to surface deformations is much higher. When looking at Equation (8) we observe that a 1-m surface displacement in range yields a phase signature of 1 m, corresponding to about 35 fringes, which can easily be measured. That means, the sensitivity of the phase difference to surface displacements in range direction is about 3000 times greater than to topography.

Applications

The potential of InSAR to map centimeter-scale ground displacements over a region many tens of kilometers in size at a resolution of a few meters, makes it one of the most promising space-geodetic techniques for monitoring deformations. It may be applied to all

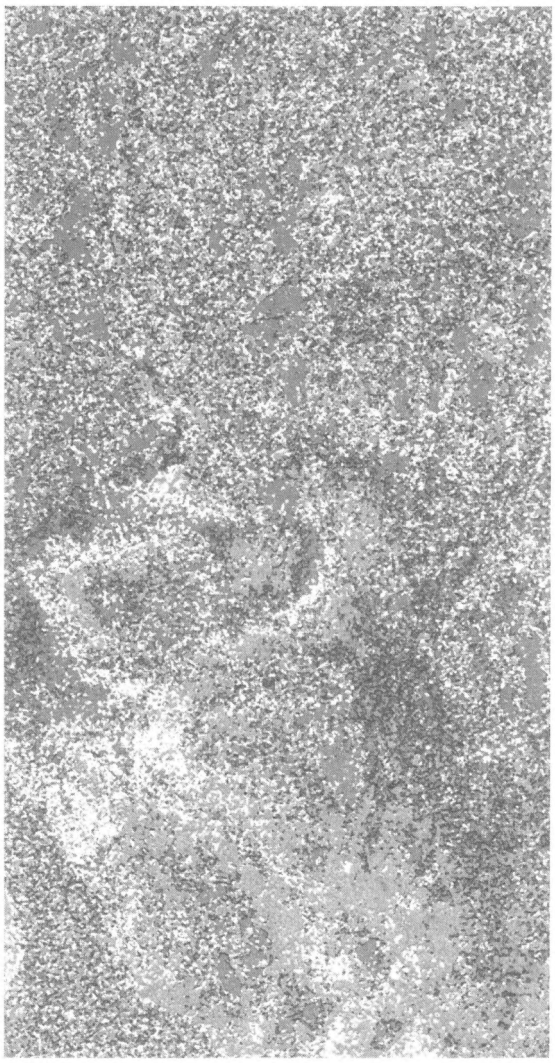

Figure 7. Deformation field of the M = 6.7, 18 June 1994, Arthur's pass earthquake in the Southern Alps of New Zealand, mapped by InSAR. North to the top; scale is 50 m a pixel; image size is 51.2 km in E–W, and 94.6 km in N–S direction. (For full colour reproduction of this figure, see Appendix at the end of this issue.)

kinds of deformation processes: land subsidence, co- and post-seismic deformations, volcano deformation, and glacier and ice-sheet dynamics. We could even think of monitoring man-made objects. For the Netherlands, interesting potential applications are the monitoring of land subsidence due to withdrawal of ground water, oil or gas, the monitoring of surface change in coastal areas and of man-made objects like dams. A few examples of these applications are presented in the following sections.

Earthquake research and crustal dynamics

The Landers, southern California, 28 June 1992, magnitude 7.3 earthquake has provided the first full-scale validation of InSAR as a geodetic technique. The ground deformation ruptured the surface up to 6 m and has been monitored using two-pass InSAR (Massonnet et al. 1993). It has triggered a wealth of other studies (Massonnet et al. 1994b, Zebker et al. 1994, Peltzer & Rosen 1995, Feigl et al. 1995, Massonnet & Feigl 1995b, Bernard et al. 1996, Meyer et al. 1996, Murakami et al. 1996). Since then, many earthquakes have been analyzed using various satellites and, sometimes, having different satellites analyzing the same site and providing various points of view (Massonnet et al. 1996a). A crucial point in the wide acceptance of this result by the geophysical community was the similarity of the interferometric result with a fake interferogram built from the surface rupture measurement assuming an elastic behavior of the crust. The Landers example was perfectly pedagogical in the sense it did not show totally unexpected results on a large scale while giving surprisingly accurate results on secondary phenomena, such as tiny fault shifts triggered by the main shock, the kind of phenomena for which this field of study was started at the Centre National d'Etudes Spatiales (CNES, Massonnet 1985). In particular, a shift as small as 7 mm was detected on the Garlock fault by InSAR, but not by one of the most dense geodetic network in the world (Massonnet et al. 1994b). At other places, InSAR confirmed fault shifts observed in the field.

A less typical example of an earthquake study by InSAR (Figure 7) shows the deformation caused by the Arthur's pass earthquake, which struck Arthur's pass National Park in New-Zealand (Robinson et al. 1995). The interferogram results from two SAR images of the Japanese JERS-1 satellite separated by more than two years. The images have a pretty good coherence despite the seasonal changes in this prairie-covered and forested mountainous site. One fringe corresponds to 12 cm of deformation in the radar line-of-sight direction. Despite our attempt to detect precursory displacements, none was ever recorded by InSAR yet. Part of the difficulty (assuming that such precursors exist!) is to decide whether a fringe pattern is pre-seismic or post-seismic. Relatively large post-seismic displacements have been studied recently (Massonnet et al. 1996b, Peltzer et al. 1996). This helps to understand what InSAR brings to crustal studies: the complex, near-fault patterns of post-seismic

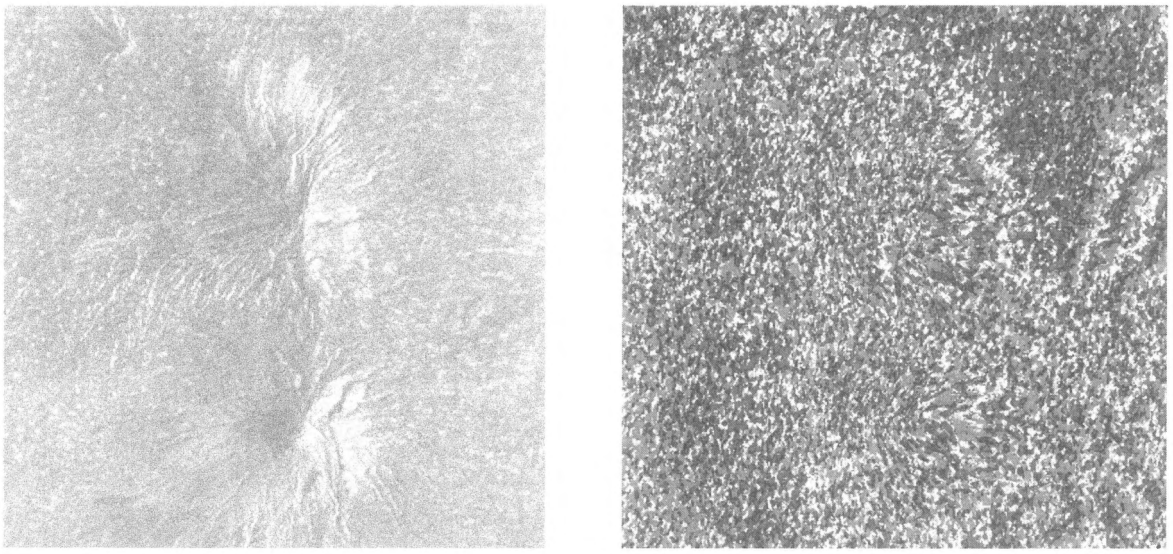

Figure 8. JERS-1 amplitude image (left) and interferogram (right) of the area around Merapi (south/bottom) and Merabu (north/top) volcanoes, near Yogyakarta in central Java, Indonesia. Scale is 40 m a pixel (no other information available to the authors). (For full colour reproduction of this figure, see Appendix at the end of this issue.)

deformation would need an impossibly dense and costly GPS network to be unambiguously mapped. While InSAR agrees with GPS measures, the latter cannot decide between various geophysical models because of the strong spatial undersampling of the deformation field. More recently, rifting processes have been observed in Iceland (Sigmundsson et al. 1997, Vadon & Sigmundsson 1997). The latest studies indicate clearly that, in some areas (Landers, Atacama, Iceland), fringes can be produced with SAR images separated by four years without noticeable loss of quality. We may therefore expect some sites to retain coherence for tens of years, an exciting prospect for crustal studies. Assuming a dedicated InSAR mission will be launched, displacements of 1 mm/yr could be mapped.

Volcano monitoring

Unlike earthquake research and crustal dynamics, volcano monitoring using InSAR offers a clear, near-term perspective in disaster prevention, because the eruption of a volcano is preceded by terrain deformation. Some additional specific points are important. Firstly, the position of volcanoes is well known and their systematic survey would require only a few hundred local digital elevation models (DEM) and a few thousand radar images per year. Secondly, the deformation is continuous rather than step-wise, and it is associated with a typical time scale of months rather than (many) years. Thirdly, although volcanic areas show often large height differences, and thus suffer from changes of atmospheric column or snow coverage at summit, the images mostly have a sufficiently high coherence, if not of top quality. The different volcanoes studied so far, whether in Iceland (Sigmundsson et al. 1997, Vadon & Sigmundsson 1997), Alaska (Lu et al. 1997), Indonesia (Figure 8), the Indian Ocean, Europe, North America (Thatcher & Massonnet 1997) or the Hawaiian Islands (Rosen et al. 1996), have all provided valuable results using various radar satellites. The first interferometric study (Massonnet et al. 1995) has revealed unknown features through the analysis of time series of interferograms of the deflation of Mount Etna during the end of its last eruption. New significant results were obtained, namely the unexpected depth of the source of deformation, in Mount Etna, one of the best surveyed volcanoes in the world. The classical geodetic techniques evidently did not indicate the regional extent of the deformation, but InSAR did. The study was followed by a more detailed analysis of the mechanisms of flank failure (Briole et al. 1997). Monitoring of volcanoes normally does not produce spectacular results as shown in a study of La Palma (Figure 9). The ERS-1 amplitude image of this island in the Atlantic ocean (Figure 9, left) clearly reveals the topographic structure of the volcano. The topographic interferogram made from two ERS-1 images separated by three years (Figure 9, right) shows noisy data in

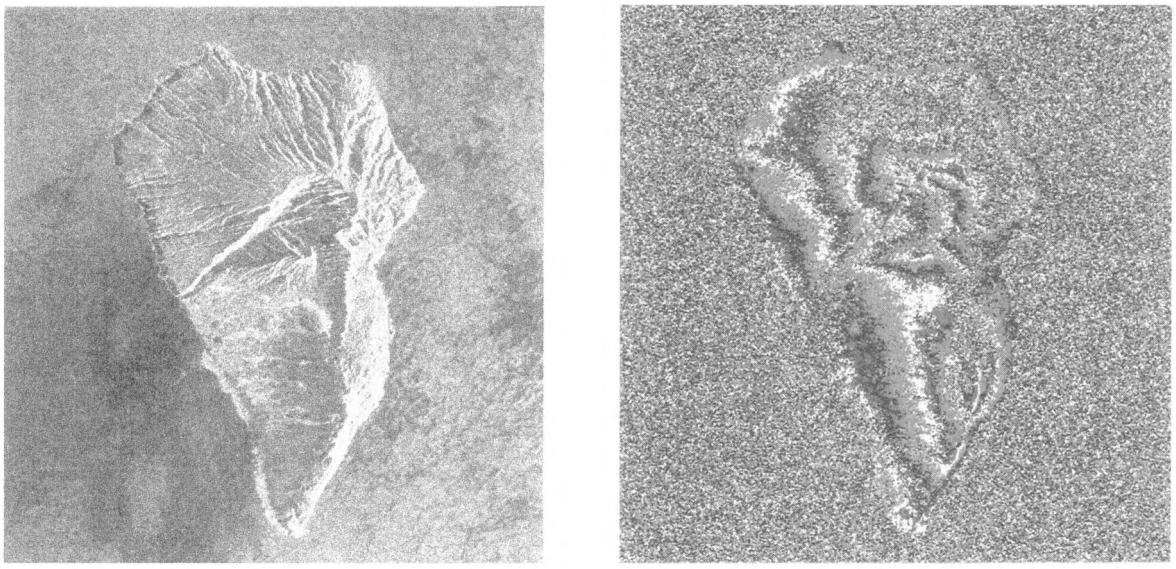

Figure 9. Amplitude image (left) and uncorrected interferogram (right) of La Palma island, Atlantic Ocean. North to the top; image size is ca. 50 × 30 km. (For full colour reproduction of this figure, see Appendix at the end of this issue.)

some parts of the island, but over most of the land surfaces the interferogram remains coherent, even after three years.

No DEM was used to correct the result, but we know that La Palma is some 3000 m high and that the altitude of ambiguity is about 1000 m. The three fringes we see on the image are clearly due to topography alone and indicate that the volcano did not inflate markedly during the three years elapsed. This illustrates a very cost-effective way to survey dormant volcanoes. The availability of a DEM would not complicate the survey technically, but make the result more obvious to decision makers.

Anthropogenic processes

Many man-made activities can generate terrain deformation with the kind of spatial extent and gradient boundaries measurable by InSAR. With that we mean an area at least several tens of pixels across (i.e. on the order of 1 km across) with a relative deformation typically lower than 10^{-3}. In this context, one can think of processes such as coal extraction and other mining activity, or of fluid extraction in geothermal plants, and last but not least oil or gas production and related subsidence. The terrain may also be deformed by underground explosions, such as in tests of nuclear weapons, or in the destruction of old mines. Man-made activities do not result exclusively in subsidence: underground gas storage and vapor-assisted oil extraction may result in soil swelling. Most of these activities have been mapped by InSAR and more or less openly discussed. Unlike the other topics addressed in this paper, man-made activities involves

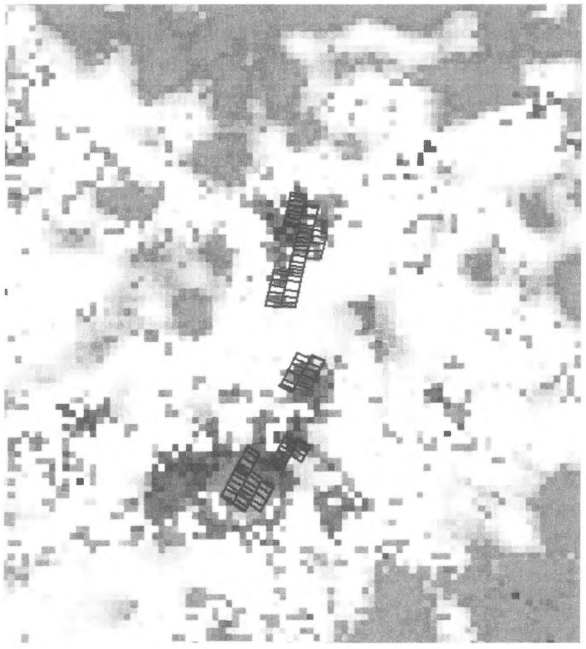

Figure 10. Close-up of interferogram of Gardanne mining site, France. The area covers ca. 8.4 × 9.4 km, the pixel size is 100 m. Superimposed is the mining schedule since 1990 (from Carnec et al. 1996). (For full colour reproduction of this figure, see Appendix at the end of this issue.)

subtle economical, strategic or even legal issues. As examples, we will focus on two specific applications. The first deals with mining near the city of Gardanne, in France, and has been reported in Carnec et al.(1996).

The subsidence in the Gardanne example (Figure 10) is best observed using two ERS-1 images separated by 35 days. The image maps precisely indicate the extent of the subsidence (roughly 2000 m across) and its deepest point, 42 mm. The data agree with previous information but allow a more accurate modeling of the mechanism. Black rectangles show the location of mining activity 1000 m below the surface. The second example deals with the East Mesa geothermal plant, located in Southern California, for which Massonnet et al. (1997) reported subsidence inadvertently detected by InSAR during a routine survey. Short-term interferograms reveal surface-phase changes on agricultural fields similar to what had been observed previously with SEASAT radar data (Gabriel et al. 1989). Long-term (2 years) interferograms allow to map and measure land subsidence and, while agreeing with existing, sparse leveling data, provides a quantitative account of the activity of the plant. The amount of water extracted from the 2000-m-deep field during two years is 100 million m^3 of which 95 have been reinjected after use, and the integration of the subsidence bowl gives 4 million m^3. Notable consequences of the subsidence can be envisaged where two canals cross the area of subsidence. The main limitation to this kind of application is the temporal decorrelation, i.e. the loss of phase coherence. The deformations are generally located in a rather flat area, which minimizes the contribution of the topography to the interferograms and their positions are generally known a priori, which greatly helps the discussion related to atmospheric artifacts, because it is very unlikely to find them repeatedly positioned on the area of interest.

Glacier and ice-sheet monitoring

With regard to glacier and ice-sheet monitoring, recent examples have demonstrated that InSAR can: a) provide high-resolution high-accuracy topographic maps of glaciers and ice sheets, b) measure ice-flow velocity without any ground control, c) detect and monitor surface changes, d) identify the line separating floating ice from grounded ice, and e) measure changes in surface-geophysical parameters (see e.g. Goldstein et al. 1993, Hartl et al. 1993, 1994, Thiel et al. 1996, Wu & Thiel 1996, Kwok & Fahnestock 1996, Lingle et al. 1997, and Joughin et al. 1997).

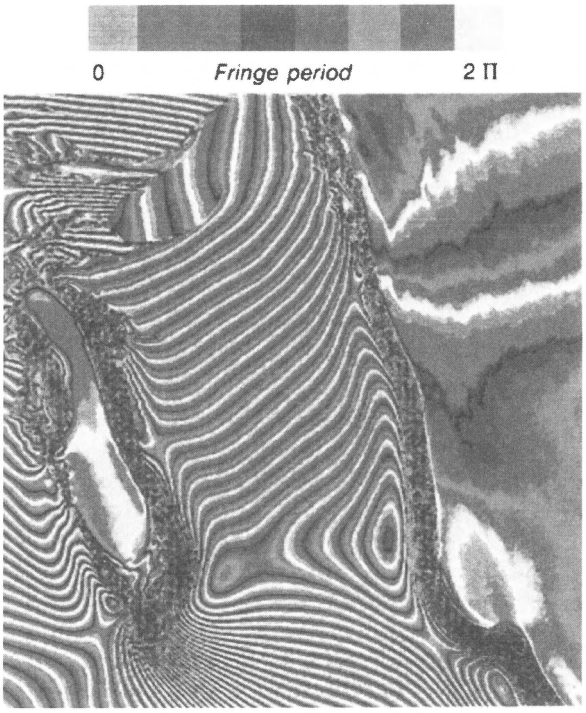

Figure 11. SAR interferogram of the Filchner-Ronne shelf ice in the Antarctic (from Hartl et al. 1994). We see on the right side the western slope of Berkner Island resting on bedrock, and on the left Hemmen Ice Rise grounded on sea-bed shoals and surrounded by the floating Ronne Ice Shelf. (For full colour reproduction of this figure, see Appendix at the end of this issue.)

An interferogram taken from Hartl et al. (1994) of the area around Hemmen Ice Rise on the Filchner-Ronne shelf ice in the Antarctic, derived from two ERS-1 SAR images acquired at 26 and 29 January 1992, during the ERS-1 ice phase, has been reproduced in Figure 11. The fringes of the Ronne Ice Shelf reflect not only the motion of the Filchner-Ronne shelf ice over three days, but also the topography and the effect of the tides. To distinguish between these effects, further information is needed or certain assumptions have to be made. For instance, if one is interested in the tidal signal, three SAR images can be used to form two independent interferograms. Then, assuming that the topography has not changed and the ice flow was steady during data acquisition, taking the difference between the two interferograms cancels the effect of steady motion and topography, thus providing the line-of-sight deformation due to tides (Figure 12).

Severe limitations to InSAR for polar and glacier studies come from the temporal decorrelation and the

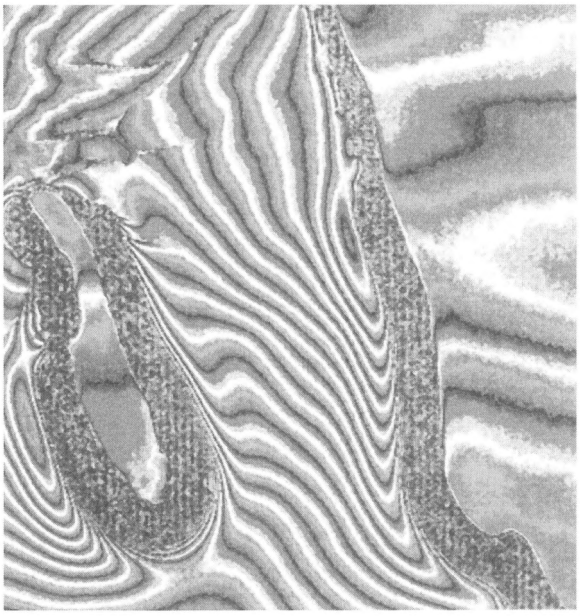

Figure 12. Differential SAR interferogram of the Filchner-Ronne shelf ice showing differences in the tidal signal at the data acquisition times (from Hartl et al. 1994). The rise and fall of the ocean tide and the seaward movement of the ice can be seen in the fringe pattern towards the top of the image. (For full colour reproduction of this figure, see Appendix at the end of this issue.)

need to separate between various effects that contribute to the fringe pattern such as ice motion, topography and tides. Changes in snow and ice conditions may yield very noisy interferograms over time scales much shorter than the repeat period of the satellite (e.g. Goldstein & Werner 1997). Additional problems arise due to the fact that InSAR only measures the line-of-sight component of the velocity vector with reasonably high accuracy and because sometimes it can be difficult to find stationary regions in the scene.

The separation of various effects and the determination of the three-dimensional velocity field normally requires more SAR images. Moreover, the latter is not possible without some assumptions. On the other hand, due to the temporal decorrelation, the number of SAR images needed to infer the required information should be as low as possible. With regard to the separation of the topography, no additional SAR images are needed if a DEM is available (e.g. Joughin et al. 1996). The same holds if the baseline is short, say, some tens of meters, and the scene is rather flat, since then the topography can be neglected (e.g. Müller et al. 1997). Otherwise, at least three SAR images with sufficiently high coherence must be available to eliminate the topography.

Since one interferogram only shows the radar line-of-sight motion, at least three observations with different orientations are needed to determine the three-dimensional velocity field. Combining successive ascending and descending SAR images can provide two observations if the crossing angle between ascending and descending orbit is not too small. In the case of ERS-1 and ERS-2 it is about 48° over the Antarctic. Usually, the missing third observation is replaced by the surface slope derived from InSAR and the assumption that the ice flow is parallel to the surface topography, i.e. in the direction of the maximum slope (e.g. Joughin et al. 1997). Then, it is possible to eliminate up to a certain extent the vertical flow component yielding the horizontal velocity in the across-track direction.

InSAR has also been applied to monitor surface-changes in ice-covered regions. For instance around the Vatnajokull volcano in Iceland, two interferograms of the area taken from Thiel et al. (1997) have been reproduced in Figure 13. The volcano erupted on 30 September 1996, after an earthquake with a magnitude of 5.4 on the Richter scale and the images have been acquired on 21 and 22 October 1996, during the ERS-1/2 tandem mission. The interferogram on the left of Figure 13 shows the fringes due to the topography and the surface deformation. After removing the effect of the topography, the remaining fringes express the surface-changes over 1 day due to the eruption (right interferogram in Figure 13). Various areas can be identified of large deformations, up to 25 fringes corresponding to 80 cm deflation within 1 day. We also see some areas which are completely decorrelated, partially because the deformations are that large that coherence is lost and no fringes show up. Although InSAR has shown to be a promising technique for monitoring glaciers and ice sheets, we are still far from exploiting its full potential. Too many problems are not yet fully solved. For instance, present satellites with a SAR as payload do not fully cover polar regions. ERS-1 and ERS-2, for example, leave a gap of about 8° at the poles. In addition, Greenland and polar regions suffer from severe weather conditions which may lead to complete decorrelation within a few days, due to snow storms, melting, blowing snow etc. Finally, atmospheric disturbances may corrupt the interferograms.

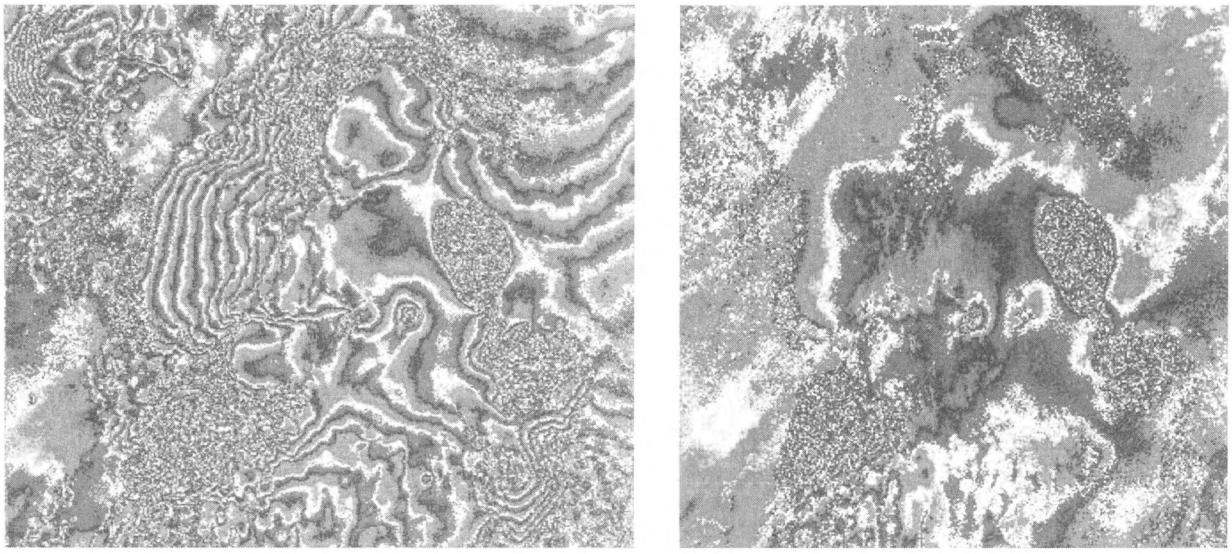

Figure 13. Interferograms of the area around Vatnajökull volcano on Iceland formed by SAR images acquired at 21 and 22 October 1996. Topography (left) and subsurface deformation (right). One fringe corresponds to ca. 72 m elevation change (left) and 3 cm vertical deformation (right), respectively (from Thiel et al. 1997). (For full colour reproduction of this figure, see Appendix at the end of this issue.)

Limitations to SAR interferometry

The use of repeat-pass InSAR for surface-change detection is mainly limited by two effects: a) the influence of the atmosphere (e.g. Van der Kooij et al. 1995, Mouginis-Mark 1995, Goldstein 1995, Hanssen & Feijt 1996, Zebker & Rosen 1997), and b) the problem of temporal decorrelation (e.g. Zebker & Villasenor 1992, Van der Kooij et al. 1995). Whereas the first produces systematic errors (bias) in surface-displacement estimates from InSAR, the latter increases the noise level and can even make interferometric phase comparison impossible due to loss of phase stability. Let us briefly address both problems.

Atmospheric perturbations

The determination of surface-changes using InSAR is based on the assumption that the radar signal propagates unaffected in the atmosphere. This, however, is not the case. Path delays occur in both the ionosphere and the troposphere. Ionospheric path delay is caused by variations in the Total Electron Content along the path and by Traveling Ionospheric Disturbances. The former depends on the time of day and influences the whole scene rather homogeneously. The latter may cause localized artifacts. The most severe atmospheric effect, however, is due to the troposphere. Its path delay consists of two components, the dominant dry part (about 2.3 m in vertical direction) and the small but highly variable wet part which is caused by the strong temporal and spatial variability of the water-vapor concentration. It can take on magnitudes up to 30 cm. Artifacts in interferograms have been reported quite often and some of them have been assigned to atmospheric perturbations as in Massonnet et al. (1994a), Massonnet & Feigl (1995a) and Hanssen & Feijt (1996). These effects can cause misinterpretation of deformation fields derived by InSAR in the order of centimeters. For instance, a differential interferometry chart of the Kilauea volcano system, generated by data of the April and October mission of SIR-C in 1994 has first been interpreted as a demonstration of a volcanic lift of several centimeters, but turned out later to be just an atmospheric effect as was reported by a team of scientists of the NASA Jet Propulsion Laboratory, Pasadena, California, on several occasions. Similar effects have been reported by Hanssen & Feijt (1996). Although recognized as one of the most important and challenging research topics on InSAR, only a few quantitative results have been published so far, e.g. by Goldstein (1995), Van der Kooij et al. (1995), Massonnet & Feigl (1995a) and Tarayre & Massonnet (1996).

Especially in wet regions like the Netherlands, SAR images exhibit artifacts due to the temporal and spatial variations of atmospheric water vapor. Other tropospheric variations, such as pressure and temperature, as well as ionospheric perturbations also

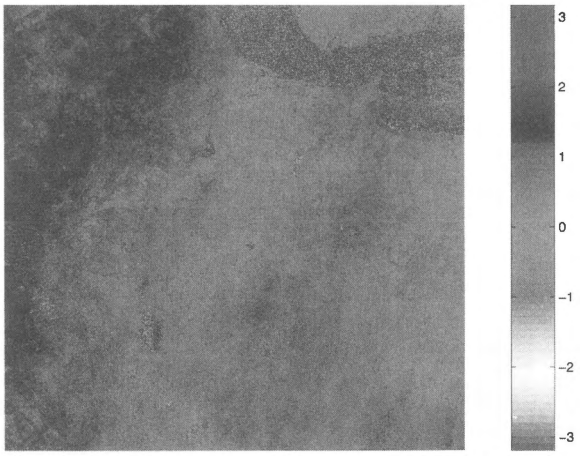

Figure 14. ERS tandem mission interferogram of the Groningen area, the Netherlands, from SAR images acquired at 26 and 27 February 1996, at 10:29 UTC (from Hanssen & Feijt 1996) showing phase changes of 11 mm. The effect of topography in this flat terrain can be almost neglected, changes due to surface deformation within a one-day period are unlikely. Therefore, the observed phase change represents disturbing effects possibly attributable to atmospheric perturbations. North to the top; image size is ca. 50 × 50 km. (For full colour reproduction of this figure, see Appendix at the end of this issue.)

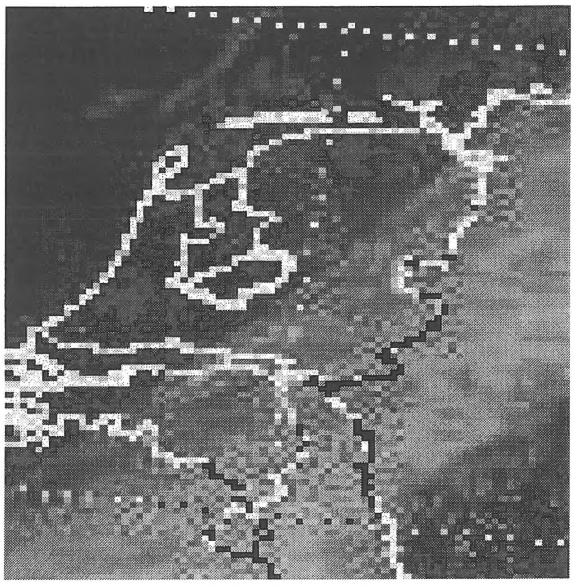

Figure 15. NOAA-AVHRR image acquired at 27 February 1996, 12:02 UTC (from Hanssen & Feijt 1996) indicating a frontal zone with high humidity passing the Groningen area. North to the top; image size is ca. 350 × 350 km.

induce distortions, but the effects are smaller in magnitude and more evenly distributed throughout the interferogram than the wet troposphere term.

As an example, an interferogram of the area of Groningen is presented in Figure 14. A phase change of about 0.4 cycles, equivalent to about 11 mm, is indicated. Since the area is almost flat, the contribution of topography to the observed phase change is negligible. The same holds true for any surface deformation because of the time interval of just one day. Thus, the observed phase change represents some disturbing effects. Because of the large-scale structure of the phase change, atmospheric perturbations are likely to be responsible. To investigate this, METEOSAT data have been acquired 3 minutes before the first of the SAR images in addition to the NOAA data acquired 2 hours later. These images acquired on 26 February, 12:14 and 10:26 UTC, respectively, do not show any irregularities. However the NOAA-AVHRR image of 27 February, 12:02 UTC, shown here in Figure 15, as well as the METEOSAT image of the same day clearly indicate a frontal zone passing the Groningen area. In the frontal zone, relative humidity is high from the ground up till several kilometers. Behind the frontal zone, the atmosphere dries out. Using vertical radio-probe profiles of temperature, pressure, and relative humidity, a path delay of 15 mm during the 24 hours in which the

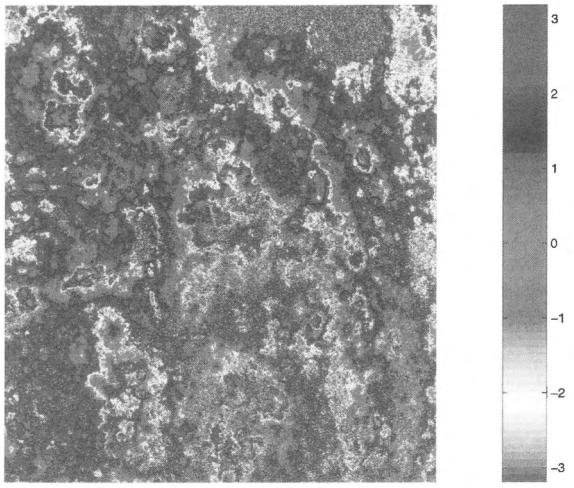

Figure 16. Interferogram of the Groningen area taken over one day. The fringe patterns indicate the influence of convective cells during data acquisition. Up to two fringes corresponding to 5.6 cm line-of-sight propagation delay can be counted showing that atmospheric effects can have a very large influence on the interferogram (from Hanssen & Usai 1997). North to the top; image size is ca. 50 × 50 km. (For full colour reproduction of this figure, see Appendix at the end of this issue.)

frontal zone passed the Groningen area, has been estimated using the tropospheric model of Saastamoinen (1972). That agrees nicely with the 11-mm estimate from the interferogram. Moreover, when comparing the phase patterns in the interferogram with the patterns in the METEOSAT and NOAA images, we see a high correlation.

A second example of the same area is shown in Figure 16. The images have been acquired during the ERS-1/2 tandem mission on two successive days and show the fringe pattern which is due to convective cells. Up to two fringes corresponding to a line-of-sight path delay of 5.6 cm can be counted showing that atmospheric effects can have a very large influence on the interferogram. Theoretical calculations show that atmospheric artifacts in SAR interferograms can even be much larger (Hanssen & Feijt 1996, Zebker & Rosen 1997). For instance, spatial and temporal changes of 20% humidity lead to 10-cm errors in deformation images. Since the effect is independent of frequency at microwave wavelength, the contamination of the signal cannot be mitigated by dual-frequency measurements such as those commonly utilized for ionospheric corrections.

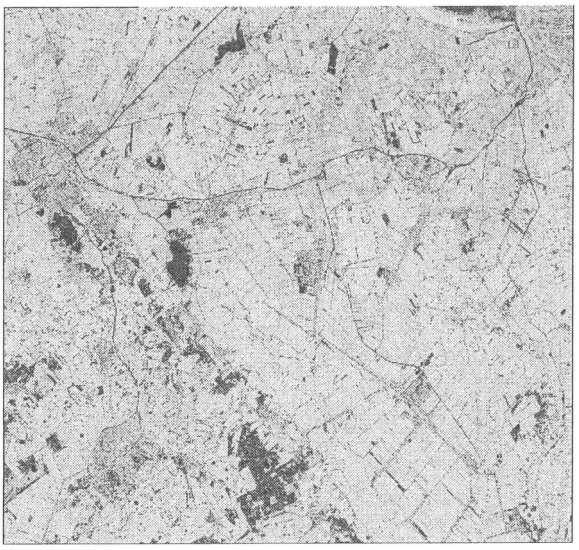

Figure 17. Coherence image for a one-day time interval of the Groningen area (from Usai & Hanssen 1997). Strong correlation can be observed over a one-day period for the entire area allowing accurate ground displacements to be measured; however, after few months, much of the correlation is lost. After 3.5 years (image not portrayed here), the scene is almost decorrelated and no surface-changes can be measured. North to the top; image size is ca. 50 × 50 km.

Temporal decorrelation

The main limiting factor for repeat-pass InSAR is the temporal change of the backscatter property of the surface in between two satellite passes, the so-called temporal decorrelation. Reasons are volume scattering in vegetated areas, especially forest, changes in vegetation, variations in soil moisture, lava flow, freezing and thawing, and man-made changes. Temporal decorrelation is the highest for water surfaces and the lowest for desert or other arid areas with low vegetation. A loss of correlation, i.e. of scene coherence, makes the gathering of sound phase information more difficult or even impossible. For instance, agricultural and other vegetated areas suffer from severe temporal decorrelation. In many SAR images, decorrelation effects are visible even after just one day (ERS tandem mission), mostly due to anthropogenic processes; after a few weeks the complete scene can be almost decorrelated.

Qualitatively, it is known that: 1) desert is better than dense forest; 2) dry conditions are better than wet; 3) long radar wavelength is better than short; 4) urban areas and solid scatterers such as houses, rocks, and corner reflectors do hardly decorrelate; 5) water decorrelates within 0.1 s which means that repeat-pass InSAR cannot be applied over ocean surfaces; and 6) human agricultural activities lead to a complete loss of coherence for individual agricultural fields. Present research focuses on the use of 'single' scatterers, which very often can be identified in otherwise decorrelated images. They might be phase stable even over years and may carry the information on the surface-change which has to be extracted.

Temporal decorrelation in the area of Groningen is here shown as an example over a period of one day and 3.5 years (Figure 17). Over one day most of the area remains strongly correlated, and a phase comparison can be done to determine ground displacements with high accuracy and reliability. However, already after two months, large parts of the scene correlation is lost, and a phase comparison seems to be doubtful to perform. After 3.5 years (image appears entirely black), the scene is almost decorrelated, and the extraction of any information seems to be hopeless. Nonetheless, there is still a large number of objects, mainly in urban areas, with high coherence over long time periods. An actual point of research is whether or not we can make use of these 'fixed' objects to gain information on the deformation process over longer time scales. Increasing the coherence estimation window allows to better discriminate between areas of different co-

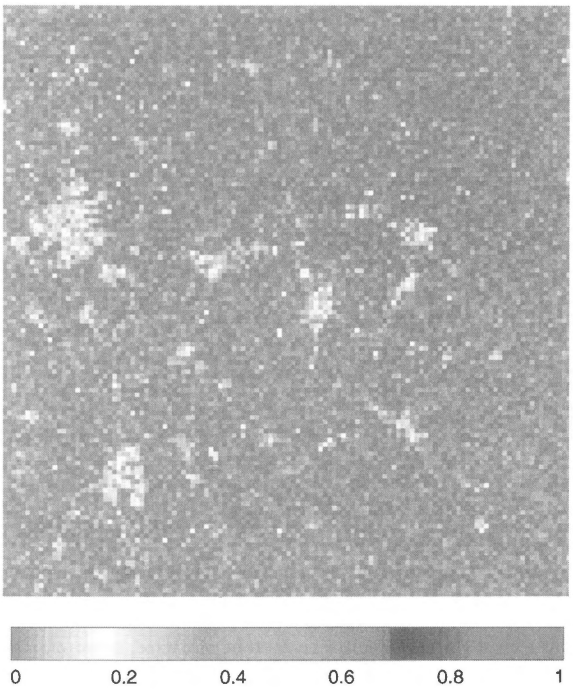

Figure 18. Coherence image for the Groningen area shown in Figure 16, for 3.5 years using 20 × 110 independent samples per pixel. The image pair contains information which may be used to extract phase values (from Hanssen & Usai 1997). North to the top; image size is ca. 50 × 50 km. (For full colour reproduction of this figure, see Appendix at the end of this issue.)

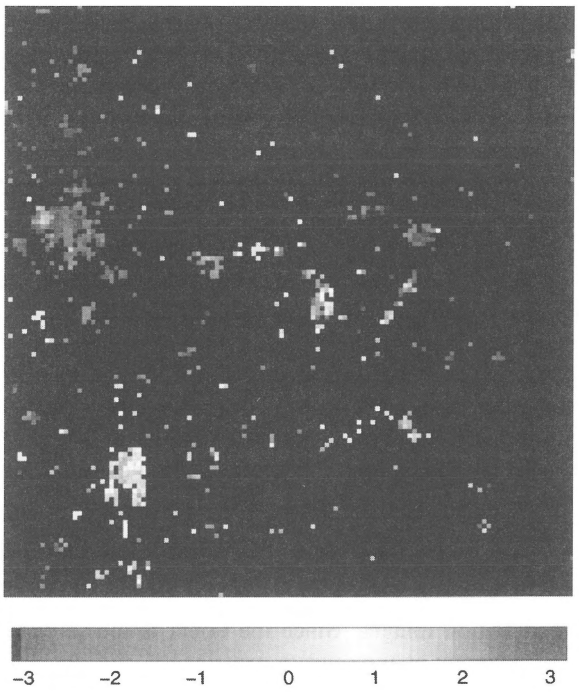

Figure 19. Masked interferogram for the Groningen area shown in Figure 16 (threshold 0.1) for a multilook window of 20 by 110 pixels (from Hanssen & Usai 1997) showing that the extraction of deformation signature is possible by eliminating those pixels with high satellite orbit errors and with disturbance due to atmospheric perturbations. North to the top; image size is ca. 50 × 50 km. (For full colour reproduction of this figure, see Appendix at the end of this issue.)

herence. Figure 18 shows the coherence for the same 3.5-year time interval with a coherence estimation window of 20 × 110 pixels. Clearly, the image pair still seems to contain information which may be used to extract reliable phase values. The interferometric phase values where the coherence is higher than 0.1 is shown in Figure 19. The extraction of the deformation signature would be possible if other potential contributions to the phase values could be separated such as satellite orbit errors and atmospheric perturbations.

Concluding, temporal decorrelation is a serious problem for the monitoring of deformation processes with sufficient confidence, especially when long time series are needed.

Summary

InSAR is a powerful space-geodetic technique for surface-change detection with a huge number of potential new applications in the fields of land-subsidence monitoring, crustal dynamics, earthquake research, volcanic monitoring, and glacier and polar-ice studies. Although rather new and not yet fully exploited, it has already generated an enormous interest in the earth-science community. A dedicated InSAR mission with well-designed instruments and some supporting sensors would provide a unique tool for long-term monitoring of active volcanoes, seismic areas, continental glaciers and ice sheets and other surface-change phenomena such as land subsidence due to mining activities and withdrawal of water, gas, and oil. However, some factors limit the applications of InSAR such as the temporal sampling, the geometric constraints, the atmospheric perturbations, and the problem of temporal decorrelation. Therefore, InSAR has to be regarded as complementary to already existing space-geodetic techniques. Together they will substantially extend the contribution of geodesy to earth sciences and global-change studies.

References

Bernard, P., P. Briole, B. Meyer, H. Lyon-Caen, J.M. Gomez, C. Tiberi, C. Berge, D. Hatzfeld, C. Lachet, B. Lebrun, A. Deschamps, F. Courboulex, C. Laroque, A. Rigo, D. Massonnet, P. Papadimitriou, J. Kassaras, D. Diagourtas, K. Makropoulos, G. Veis, E. Papazisi, C. Mitsakaki, V. Karakostas, E. Papadimitriou & D. Papanastassiou 1996 The M = 6.2 June 15, 1995 Aigion earthquake (Greece): results of a multidisciplinary study – J. Seismol. 1: 131–150

Briole, P., D. Massonnet & C. Delacourt 1997 Post-eruptive deformation associated with the 1986–87 and 1989 lava flows of Etna, detected by radar interferometry – Geoph. Res. Lett. 24: 37–40

Carnec, C., D. Massonnet & C. King 1996 Two examples of the application of SAR interferomety to sites of small extent – Geoph. Res. Lett. 23: 3579–3582

Dixon, T. (ed.) 1995 SAR interferometry and surface-change detection. University of Miami Technical Report TR 95–003, Miami, 97 pp

Feigl, K., A. Sergent & D. Jacq 1995 Estimation of an earthquake focal mechanism from a satellite radar interferogram: application to the December 4, 1992 Landers aftershock – Geoph. Res. Lett. 22: 1037–1048

Gabriel, A., R.M. Goldstein & H.A. Zebker 1989 Mapping small elevation changes over large areas: differential radar interferometry – J. Geophys. Res. 94: 9183–9191

Goldstein, R. 1995 Atmospheric limitations to repeat-track radar interferometry – Geoph. Res. Lett. 22: 2517–2520

Goldstein, R. & C. Werner 1997 Radar ice motion interferometry. In: Proc. 3rd ERS Symposium 'Space at the service of our environment', Florence, Italy, 17–21 March, 1997, ESA Publications, Noordwijk, SP 414, II: 963–972

Goldstein, R., H. Engelhardt, B. Kamb & R. Frolich 1993 Satellite radar interferometry for monitoring ice sheet motion: application to an Antarctic ice stream – Science 262: 1525–1530

Hanssen, R. & A. Feijt 1996 A first quantitative evaluation of atmospheric effects on SAR interferometry. In: Proc. FRINGE 96 Workshop on ERS SAR Interferometry, Zürich, Switzerland, 30 Sept–2 Oct. 1996, ESA Publications, Noordwijk, SP 406, 1: 277–282

Hanssen, R. & S. Usai 1997 Interferometric phase analysis for monitoring slow deformation processes. In: Proc. 3rd ERS Symposium 'Space at the Service of our Environment', Florence, Italy, 17–21 March, 1997, ESA Publications, Noordwijk, SP 414, I: 487–492

Hartl, P., K.-H. Thiel & X. Wu 1993 Information extraction from ERS-1 SAR data by means of INSAR and D-INSAR techniques in Antarctic research. In: Proc. 2nd ERS Symposium, Hamburg: 697–702

Hartl, P., K.-H. Thiel, X. Wu, C. Doake & J. Sievers 1994 Application of SAR interferometry with ERS-1 in the Antarctic – Earth Observ. Quarterly 43: 1–4

Joughin, I., R. Kwok & M. Fahnestock 1996 Estimation of ice-sheet motion using satellite radar interferometry – method and error analysis with application to Humboldt glacier, Greenland – J. Glaciology 42: 564–575

Joughin, I., R. Kwok, M. Fahnestock, D. Winebrenner, S. Tulaczyk & P. Gogenini 1997 Interferometric estimation of ice sheet motion and topography. In: Proc. 3rd ERS Symposium 'Space at the Service of our Environment', Florence, Italy, 17–21 March 1997, ESA Publications, Noordwijk, SP 414, II: 973–978

Kwok, R. & M.A. Fahnestock 1996 Ice sheet motion and topography from radar interferometry – IEEE Trans. Geosci. Rem. Sens. 34: 189–200

Lingle, C., D. Fatland, V. Voronina, K. Ahlnäs & E. Troshina, E. 1997 Dynamic behaviour of the Bering Glacier-Bagley icefield system during a surge, and other measurements of Alaskan glaciers with ERS SAR imagery. In: Proc. 3rd ERS Symposium 'Space at the Service of our Environment', Florence, Italy, 17–21 March 1997, ESA Publications, Noordwijk, SP 414, II: 995–1000

Lu, Z., R. Fatland, M. Wyss, S. Li, J. Eichelberger, K. Dean & J. Freymueller 1997 Deformation of New Trident Volcano measured by ERS-1 SAR Interferometry. Katmai National Park, Alaska – Geoph. Res. Lett. 24: 695–698

Massonnet, D. 1985 Etude de principe d'une detection de mouvements tectoniques par radar – Centre National d'Etudes Spatiales Internal Memo 326, Toulouse: 20 pp

Massonnet, D. & K.L. Feigl 1995a Discriminating geophysical phenomena in satellite radar interferograms – Geoph. Res. Lett. 22: 1537–1540

Massonnet, D. & K.L. Feigl 1995b Satellite radar interferometric map of the coseismic deformation field of the M = 6.1 Eureka Valley, California earthquake of May 17, 1993 – Geoph. Res. Lett. 22: 1541–1544

Massonnet, D., M. Rossi, C. Carmona, F. Adragna, G. Peltzer, K. Feigl & T. Rabaute 1993 The displacement field of the Landers earthquake mapped by radar interferometry – Nature 364: 138–142

Massonnet, D., F. Adragna & M. Rossi 1994a CNES General-Purpose SAR Correlator – IEEE Trans. Geosci. Rem. Sens. 32: 636–643

Massonnet, D., K.L. Feigl, M. Rossi & F. Adragna 1994b Radar interferometric mapping of deformation in the year after the Landers earthquake – Nature 369: 227–230

Massonnet, D., P. Briole & A. Arnaud 1995 Deflation of Mount Etna monitored by spaceborne radar interferometry – Nature 375: 567–570

Massonnet, D., K.L. Feigl, H. Vadon & M. Rossi 1996a Coseismic deformation field of the M = 6.7 Northridge, California earthquake of January 17, 1994 recorded by two radar satellites using interferometry – Geoph. Res. Lett. 23: 969–972

Massonnet, D., W. Thatcher & H. Vadon 1996b Detection of postseismic fault zone collapse following the Landers earthquake – Nature 382: 612–616

Massonnet, D., T. Holzer & H. Vadon 1997 Land subsidence caused by the East Mesa geothermal field, California, observed using SAR interferometry – Geoph. Res. Lett. 24: 901–904

Meyer, B., R. Armijo, D. Massonnet, J. de Chabalier, C. Delacourt, J. Ruegg, J. Achache, P. Briole & D. Papanastassiou 1996 The 1995 Grevena (Northern Greece) Earthquake: Fault model constrained with tectonic observations and SAR interferometry – Geoph. Res. Lett. 23: 2677–2680

Mouginis-Mark, P. 1995 Analysis of volcanic hazards using Radar Interferometry – Earth Observ. Quarterly 44: 6–10

Müller, U., J. Sievers & H. Walter 1997 SAR data exploitation for monitoring antarctic ice sheets and glaciers. In: Proc. 3rd ERS Symposium 'Space at the Service of our Environment', Florence, Italy, 17–21 March, 1997, ESA Publications, Noordwijk, SP 414, II: 877–886

Murakami, M., M. Tobita, T. Saito & H. Masharu 1996 Coseismic crustal deformations of the 1994 Northridge, California earthquake detected by interferometric analysis of SAR images acquired by the JERS-1 satellite – J. Geophys. Res. 101: 8605–8614

Peltzer, G. & P. Rosen 1995 Surface displacement of the 17 May 1993 Eureka Valley, California earthquake observed by SAR interferometry – Science 268: 1333–1336

Peltzer, G., P. Rosen, F. Rogez & K. Hudnut 1996 Postseismic rebound in fault stopovers caused by pore fluid flow – Science 273: 1202–1204

Robinson, R., T. Arnadottir, J. Beavan, J. Cousins, C. Pearson, M. Reyners, R. van Dissen & T. Webb 1995 The M = 6.7 Arthur's Pass earthquake in the Southern Alps of New Zealand, June 18, 1994 – Seismol. Res. Lett. 66: 11–13

Rosen, P., S. Hensley, H.A. Zebker, F.H. Webb & E.J. Fielding 1996 Surface deformation and coherence measurements of Kilauea volcano, Hawaii, from SIR-C radar interferometry – J. Geophys. Res. 101(E10): 109–125

Saastamoinen, J. 1972 Contributions to the theory of atmospheric refraction – Bull. Géodésique 105: 106–114

Sigmundsson, F., H. Vadon & D. Massonnet 1997 Readjustment of the Krafla spreading segment to crustal rifting measured by Satellite Radar Interferometry – Geoph. Res. Lett. 24: 1843–1846

Tarayre, H. & D. Massonnet 1996 Atmospheric propagation heterogeneities revealed by ERS-1 interferometry – Geoph. Res. Lett. 23: 989–992

Thatcher, W. & D. Massonnet 1997 Crustal Deformation at Long Valley Caldera, Eastern California, 1992–1996, Inferred from Satellite Radar Interferometry – Geoph. Res. Lett. 24: 2519–2522

Thiel, K.-H., P. Hartl & X. Wu 1996 Monitoring the ice movements with ERS SAR interferometry in the antarctic region. In: Proc. 2nd ERS Applications Workshop, London: 219–223

Thiel, K.-H., X. Wu & P. Hartl 1997 ERS-Tandem-interferometric observation of volcano activities in Iceland. In: Proc. 3rd ERS Symposium 'Space at the service of our environment', Florence, Italy, 17–21 March, 1997, ESA Publications, Noordwijk, SP 414, I: 475–480

Usai, S. & R. Hanssen 1997 Long time scale INSAR by means of high coherence features. In: Proc. 3rd ERS Symposium 'Space at the service of our environment', Florence, Italy, 17–21 March, 1997, ESA Publications, Noordwijk, SP 414, II: 225–228

Vadon, H. & F. Sigmundsson 1997 Crustal Deformation from 1992 to 1995 at the MidAtlantic Ridge, Southwest Iceland, Mapped by Satellite Radar Interferometry – Science 275: 193–197

Van der Kooij, M., D. van Halsema, W. Groenewoud, G. Mets, B. Overgaauw & P. Visser 1995 SAR Land Subsidence Monitoring. Netherlands Remote Sensing Board (BCRS) Technical Report NRSP-2 95–13, Delft, 125 pp

Wu, X. & K.-H. Thiel 1996 The use of tandem data in the Antarctic area. In: Proc. FRINGE 96 workshop on ERS SAR Interferometry, Zürich, Switzerland, 30 Sept.–2 Oct., 1996, ESA Publications, Noordwijk, SP 406, II: 139–148

Zebker, H. & P. Rosen 1997 Atmospheric artifacts in interferometric SAR surface deformation and topographic maps – J. Geophys. Res. 102(B4): 7547–7563

Zebker, H. & J. Villasenor 1992 Decorrelation in interferometric radar echoes – IEEE Trans. Geosci. Rem. Sens. 30: 950–959

Zebker, H., P. Rosen, R.M. Goldstein, A. Gabriel & C.L. Werner 1994 On the derivation of coseismic displacement fields using differential radar interferometry: the Landers earthquake – J. Geophys. Res. 99: 19617–19634